HHS Public Access

Author manuscript

Sens Actuators B Chem. Author manuscript; available in PMC 2017 November 01.

Published in final edited form as:

Sens Actuators B Chem. 2016 November 1; 235: 154–161. doi:10.1016/j.snb.2016.04.179.

Ultrasonic Transducer-Guided Electrochemical Impedance Spectroscopy to Assess Lipid-Laden Plaques

Jianguo Ma[a,b], **Yuan Luo**[c], **René R. Sevag Packard**[a,b], **Teng Ma**[d], **Yichen Ding**[a,b], **Parinaz Abiri**[a,b], **Yu-Chong Tai**[c], **Qifa Zhou**[d], **Kirk K. Shung**[d], **Rongsong Li**[a,b], and **Tzung Hsiai**[a,b,c,*]

[a]Department of Bioengineering, School of Engineering and Applied Sciences, University of California, Los Angeles, CA 90095, USA

[b]Division of Cardiology, Department of Medicine, School of Medicine, University of California, Los Angeles, CA 90095, USA

[c]Department of Electrical Engineering, California Institute of Technology, Pasadena, CA 91125, USA

[d]Department of Biomedical Engineering and Cardiovascular Medicine, University of Southern California, Los Angeles, CA 90089, USA

Abstract

Plaque rupture causes acute coronary syndromes and stroke. Intraplaque oxidized low density lipoprotein (oxLDL) is metabolically unstable and prone to induce rupture. We designed an intravascular ultrasound (IVUS)-guided electrochemical impedance spectroscopy (EIS) sensor to enhance the detection reproducibility of oxLDL-laden plaques. The flexible 2-point micro-electrode array for EIS was affixed to an inflatable balloon anchored onto a co-axial double layer catheter (outer diameter = 2 mm). The mechanically scanning-driven IVUS transducer (45 MHz) was deployed through the inner catheter (diameter = 1.3 mm) to the acoustic impedance matched-imaging window. Water filled the inner catheter to match acoustic impedance and air was pumped between the inner and outer catheters to inflate the balloon. The integrated EIS and IVUS sensor was deployed into the ex vivo aortas dissected from the fat-fed New Zealand White (NZW) rabbits (n=3 for fat-fed, n= 5 normal diet). IVUS imaging was able to guide the 2-point electrode to align with the plaque for EIS measurement upon balloon inflation. IVUS-guided EIS signal demonstrated reduced variability and increased reproducibility ($p < 0.0001$ for magnitude, $p < 0.05$ for phase at < 15 kHz) as compared to EIS sensor alone ($p < 0.07$ for impedance, $p < 0.4$ for phase at < 15 kHz). Thus, we enhanced topographic and EIS detection of oxLDL-laden plaques via a catheter-based integrated sensor design to enhance clinical assessment for unstable plaque.

*Corresponding Author: Tzung K. Hsiai, M.D., Ph.D., Department of Medicine (Cardiology) and Bioengineering, University of California, Los Angeles, 10833 Le Conte Ave., CHS17-054A, Los Angeles, CA 90095-1679, thsiai@mednet.ucla.edu, Telephone: 310-268-3839.

Keywords

Ultrasonic transducers; Flexible 2-point electrode; Electrochemical Impedance Spectroscopy; Dual sensor-based intravascular catheter; Plaque assessment

1 Introduction

Plaque rupture is the primary mechanism underlying acute coronary syndromes and stroke [1–5]. Despite the advent of computed tomographic (CT) angiography, high resolution MRI [6], intravascular ultrasound (IVUS) [7, 8], near-infrared fluorescence [9], and time-resolved laser-induced fluorescence spectroscopy [10], real-time detection of the atherosclerotic lesions prone to rupture remains an unmet clinical challenge [11, 12]. In this context, we seek to establish an integration of sensing modalities, IVUS and electrochemical impedance spectroscopy (EIS) for detection of the metabolically unstable lesions.

Our laboratory has demonstrated that endoluminal EIS distinguishes pre-atherogenic lesions associated with oxidative stress in fat-fed New Zealand White (NZW) rabbits [13–17]. Specifically, vessel walls harboring oxidized low density lipoprotein (oxLDL) exhibit distinct EIS signals [17]. We revealed that oxLDL and foam cell infiltration in the subendothelial layer engendered an elevated frequency-dependent EIS by using concentric bipolar microelectrodes [17]. We validated specific electric elements to simulate working and counter electrodes at the electrode-endoluminal tissue interface [15]. We further established the application of EIS strategy to detect oxLDL-rich fibroatheroma using explants of human coronary, carotid, and femoral arteries [15]. The regions of elevated EIS correlated with intimal thickening detected via high-frequency (60 MHz) IVUS imaging and by prominent oxLDL staining [18].

In addition to the electrochemical (EIS) strategy, alternative techniques have been developed to assess the thin-cap fibroatheroma [5, 19, 20] and intraplaque angiogenesis [21–23] for plaque vulnerability. Integrated IVUS and optical coherence tomography (OCT) catheter was developed to acquire high resolution thin fibrous cap and the underlying necrotic core simultaneously [24]. Whereas the incremental imaging data helps determine the characteristics of plaque, the OCT technique is limited by the need for saline solution flushing [24]. Photoacoustics utilizes the high photo-absorption and thermal expansion of blood, and has been applied to visualize angiogenesis [25–27]. Intravascular photoacoustics enables to image vasa vasorum and intraplaque micro-vessel visualization [28–30]. However, the heat generated from thermal expansion poses an adverse effect on the vulnerable plaque [31]. Similar to OCT, saline solution flushing to remove red blood cells in aorta is essential [28]. The advent of near-infrared fluorescence (NIRF) provides cysteine protease activity as an indicator of inflammation [32], and the use of glucose analogue [^{18}F]-fluorodeoxyglucose (^{18}FDG) reveals metabolic activity by positron emission tomography (PET) [33]. However, injection of contrast agents is required for NIRT and radioactive isotopes PET imaging. Acoustic angiography [34, 35] excites at fundamental frequency and detects super-harmonics of microbubble contrast agents [36, 37] that were carried to micro-vessels by circulation. Dual frequency intravascular ultrasound transducers [38, 39] were

designed [40] to visualize the vasa vasorum and intraplaque vasculature. The acoustic angiography techniques benefited from large penetration depth and free of heating. Occlusion of blood flow followed by saline flushing is also indicated if the harmonic signal is highly scattered by microbubbles in aorta. The dual frequency IVUS also enabled to image the thin-cap fibroatheroma at the high frequency (30 MHz) and image the oxLDL at the low frequency (6.5 MHz) [38].

In this context, we seek to integrate both IVUS imaging and EIS measurements to characterize the metabolically active, albeit non-obstructive lesions when patients are undergoing diagnostic angiogram or primary coronary intervention. Rupture-prone plaques consist of oxLDL and necrotic core with low conductivity. When alternating current (AC) is applied to a plaque, the oxLDL-rich lesion is analogous to a capacitance component, exhibiting both elevated electrical impedance magnitude and negative phase. The divergence of electrical impedance between the oxLDL-laden plaque and healthy vessel provides a sensitive and specific assessment of atherosclerotic lesions. We developed a catheter-based 2-point micro-electrode configuration for intravascular deployment in NZW rabbits [41]. An array of 2 flexible rectangular electrodes, 3 mm in length by 300 μm in width, and separated by 300 μm, was microfabricated and mounted on an inflatable balloon catheter for EIS measurement of oxLDL-rich lesions. Upon balloon inflation by air pressure, the 2-point electrode array conformed to the arterial wall to with alternating current (AC) excitation. The frequency sweep from 100 – Hz 300 kHz generated distinct changes in both impedance (Ω) and phase (ϕ) in relation to varying degrees of intraplaque oxLDL burden in the aorta [41].

IVUS imaging visualizes the endoluminal surface, eccentricity of the plaque, intraplaque echogenicity and arterial wall thickness [42]. The mechanically scanning IVUS transducer (20~45 MHz) or the radial array transducer (10~20 MHz), transmitting and receiving the high frequency ultrasonic waves, is capable of delineating the cross-sectional anatomy of coronary artery wall in real time with 70 to 200 μm axial resolution, 200 to 400 μm lateral resolution, and 5 to 10 mm imaging depth [43, 44]. For these advantages, simultaneous IVUS-guided EIS measurement enabled precise alignment of the visualized plaques with the balloon-inflatable EIS sensor; thereby, providing both topological and biochemical information of the plaque (Figure 1). We performed ex vivo assessment of NZW rabbit aortas after 8 weeks of high-fat diet, and demonstrated significant reproducible measurements in both impedance and phase (p-value < 0.05) via IVUS-guided EIS assessment. Thus, our integrated sensor design enhanced IVUS-visualized plaques and EIS-detected oxLDL to assess metabolically unstable plaques.

To enhance the specificity, we have hereby established a dual sensing modalities, integrating ultrasound (IVUS) and electrochemical impedance (EIS) for detection of the mechanically and metabolically unstable lesions (Table 1). The integrated sensing modalities allow initial identification and visualization by IVUS, then electrochemical characterization by EIS. Unlike the aforementioned techniques, the IVUS-guided EIS assesses the biochemical property of plaques without the need to perform occlusion flushing.

2 Methods

2.1 Integrated sensor design

Built on our prior intravascular techniques [18, 45], the catheter-based dual sensors cannulate through aortas to reach the lesion sites for detection (Figure 1A). While advancing, the balloon (Advanced Polymers, Salem, NH, USA) is deflated (inset of Figure 1A) and the whole diameter of the sensor is 2.3 mm. When the sensor reaches the detecting sites, the IVUS transducer scans the section of aorta through the imaging window by rotating and pulling-back. In case lesion sites are detected, the whole sensor is further advanced and rotated to align the EIS sensor at the lesion sites. Air is then pumped though the outer catheter to inflate the balloon, allowing the 2-point electrode to make contract with the lesions. EIS measurement is performed and the impedance characteristics indicate the presence or absence of intraplaque lipid (oxLDL). These sequential steps effectively minimized the interference between the EIS sensor the IVUS acoustic pathway.

Performance of the integrated sensor was established by the IVUS-visualized endolumenal plaque and EIS-detected intraplaque oxLDL (Figure 1B). The two sensors were intravascularly deployed by two layers of catheters bonded together at the end of the outer layer. The 45 MHz IVUS transducer [46] was enclosed in the inner catheter with an imaging window while the EIS sensor was affixed to a balloon that was anchored on the outer catheter. The inner catheter was designed to be longer than the outer catheter by ~2 – 10 cm for the IVUS imaging window.

The IVUS imaging process required the acoustic wave to reach aorta walls and echo back to the IVUS transducer. For this reason, the inner catheter was acoustically transparent with matched impedance and low attenuation; thereby, allowing for acoustic wave penetration. The acoustic impedance match was established by two strategies: 1) water or phosphate-buffered saline (PBS) was injected into the inner catheter, and 2) the IVUS catheter was longer than the outer catheter by 2 – 10 cm (preset length) to avoid the balloon or the outer catheter from obstructing the acoustic path. PBS is fill in the inner catheter before cannulating, and then the proximal opening is sealed to maintain the PBS for the acoustic impedance matching. The IVUS transducer scans the aorta by rotation and pullback inside the inner catheter (outer diameter = 1.3 mm). The transducer is navigated by a torque wire. The flexibility of IVUS transducer torque wire allows for deployment into the inner catheter. The optimal EIS signal was demonstrated by inflating the balloon, allowing the 2-point electrode array to be in transient contact with the lumen. The balloon was mounted on the outer catheter (outer diameter = 2 mm and inner diameter = 1.7 mm).

2.2 Principles of EIS

EIS is the macroscopic representation of the electric field and current density distribution within the specimen being tested (Figure 2). Applying quasi-electrostatic limits to Maxwell's equations, the field distribution can be described as follows [47]:

$$\nabla \cdot (\sigma^* \nabla \varphi) = 0, \quad (1)$$

where $\sigma^* = \sigma_T + j\omega\varepsilon_T$. σ_T and ε_T denotes the conductivity and permittivity of the sample, respectively, ω the angular frequency, $j=\sqrt{-1}$, and φ the voltage distribution. Current density, $\vec{J} = \sigma^* \vec{E}$, is calculated with the distribution of electric field, $\vec{E}$. According to Maxwell's equations, electrical impedance of the sample, Z, is expressed as follows:

$$Z=\frac{\Delta\varphi}{\int_S \vec{J}\cdot \mathrm{d}\,\vec{S}}, \quad (2)$$

where $\vec{S}$ denotes the electrode-tissue interface area, and $\Delta\varphi$ the voltage difference across the two electrodes of the EIS sensor. The resistance and reactance value of the impedance is represented as a resister, R, and a capacitor, C (Figure 2A). Contact impedance, Z_C, at the interface between the electrode and tissue, is not negligible in most cases, and is taken into account in the measuring system as previously reported [18, 45].

The electrochemical impedance signal consists of both magnitude and phase information (Figure 2D). The low conductivity of oxLDL is the basis for an elevated magnitude in impedance in the oxLDL-laden plaques. In contrast, the high conductivity of healthy aorta walls exhibits lower impedance magnitude in response to the alternating current (AC). The complex impedance of the tissue is expressed as:

$$Z=\left(\frac{1}{j\omega C}//R\right)=\frac{R-j\omega CR^2}{1+\omega^2C^2R^2}, \quad (3)$$

$$|Z|=\frac{R}{\sqrt{1+\omega^2C^2R^2}}, \quad (4)$$

$$\phi=-\arctan(\omega CR), \quad (5)$$

where ω is the angular frequency; and ϕ the phase.

Two-point electrode EIS sensor was designed for a high specific measurement with deep tissue penetration [41]. The EIS sensor is flexible but non-stretchable, which bends with the balloon while keep the sensor dimension and remain robust. Miniature sensor width is preferable to minimize the interference to balloon inflation and to enhance the spatial specificity. The dimension along the catheter less limited, therefore, the EIS sensor was long in this dimension to benefit from high current and low noise. Both electrodes of the EIS sensor were 3 mm × 0.3 mm, and were aligned in parallel with 0.3 mm gap in between (inset of Figure 1B & Figure 2). The 2-electrode sensor design minimized the number of electrodes and maximized the gap, resulting in a deep electromagnetic field penetration into tissue. The EIS sensor were made electrical contact to the plaques upon balloon inflation.

During EIS assessment, AC current was driven through the plaque while maintaining a constant peak voltage. The current was recorded to calculate the electromagnetic impedance of the plaque in terms of impedance magnitude and phase (example in Figure 2D). By swiping the frequency, and impedance spectrum was acquired.

The flexible EIS sensor was fabricated on the polyimide substrate. First, copper (12 μm) was deposited on the polyimide (12 μm) via plated-through-hole (PTH). Subsequently, the copper was selectively removed by chemical etching based on lithographically-defined pattern using dry film photoresist. A subsequent lamination was done to cover majority of the copper area with a second layer of polyimide (12 μm), while leaving the sensor area exposed. Finally, Au/Ni (200 nm/20 nm) was immersion coated to the exposed electrodes. The polyimide substrate is not stretchable, which ensures the EIS sensor free from cracking or discontinuities. The leading wires (30 cm long) were copper layers fabricated together with the sensor and covered by the second polyimide layer. The proximal end of the leading wires was connected to Series G 300 Potentiostat (Gamry Instruments Inc., PA, USA) for EIS measurement.

2.3 Experimental design

EIS measurements were deployed to the ex vivo aortas from NZW rabbit in the presence or absence of IVUS guidance. All animal studies were performed in compliance with the IACUC protocol approved by the UCLA Office of Animal Research, and were conducted in the UCLA translational research imaging center (TRIC) laboratory. Five control rabbits fed on a normal chow diet (n=5) and 3 age-matched high-fat fed NZW male rabbits (n=3) were analyzed [48–50]. High-fat animals were placed on a 1.5% cholesterol and 6.0% peanut oil diet (Harlan Laboratory). After 9 weeks, thoracic aorta sections were dissected for the IVUS-guided EIS measurements. The ultrasound transducer rotated in the inner catheter to acquire the cross-sectional imaging around the catheter. The ultrasonic A-lines were acquired every 0.65 degrees and 550 A-lines were acquired in each frame. After digitization, the echo signal was filtered with pass band between 10 MHz and 100 MHz.

After localizing the plaques, the balloon catheter (Figure 1A) was advanced to align with the lesion sites. The balloon was inflated at ~2 atm (~ 200 kPa), facilitating the EIS sensors in contact with the lumen or lesions for assessing the electrical impedance. The diameter of the inflated balloon (6 mm) is slightly larger than the rabbit aorta (within 5 mm). When the EIS sensor was pushed against the plaque, the EIS signal changed significantly because highly conductive blood was eliminated between the sensor and the plaque. Measurement of conductive PBS mimicked [51] the poor contact with blood between sensor and tissue/plaques (Figure 4). The EIS (especially phase) monitoring and verification process guaranteed the contact, and ensured the performance repeatability. Alternating voltage (50 mV amplitude) was applied to the 2-point electrode, and the current was measured to determine the electrical impedance at the frequency sweep from 100 Hz to 300 kHz. Similar approach was performed without IVUS guidance. Each individual measurement was repeated 5 times.

The IVUS-guided images and EIS measurements were validated by histology. The aortic segments were fixed in 4% paraformaldehyde, embedded in paraffin and serially sectioned at

5 μm for histological analyses. Lipids were identified by Hematoxylin and Eosin (H&E) staining and oxLDL-laden macrophages by F4/80 staining (monoclonal rat anti-mouse antibody, Invitrogen).

Statistical analysis quantified the significance of EIS results. Average and standard deviation demonstrated the impedance characteristics and the measurement variability. A distinct differentiation between oxLDL-laden and lesion-free aortas indicated a preferable impedance characterization. Unpaired student's t-test and analysis of variance [52] with multiple comparisons adjustment were performed. A p-value < 0.05 was considered statistically significant.

3 Results

3.1 Integrated sensor

A prototype of the integrated sensor consisted of an EIS sensor and an IVUS transducer (Figure 3). The two sensors, 2-point electrode and ultrasonic transducer, were fabricated individually, followed by integration for the catheter-based deployment to assess oxLDL-laden plaques. The IVUS transducer [46] was mounted on a rotational shaft to generate radial cross-sectional images of the aortas. Interference between the two elements was minimized by separating them spatially (Figure 3A). The IVUS transducer was positioned in the acoustic image window distal to the balloon and EIS sensor.

3.2 Intravascular ultrasound imaging

Intravascular ultrasound imaging visualized the topography of the aorta and identified the endoluminal atherosclerotic lesions. The plaques were identified by ultrasound due to their distinct scattering characteristics (IVUS imaging results in Figure 4). In the IVUS-guided measurement, the EIS sensor was steered to the endoluminal sites to assess the eccentric plaques present in the thoracic aorta. In contrast, random EIS measurements were performed without the IVUS-guidance to compare variability and reproducibility.

3.3 Electrochemical impedance spectroscopy

In both the IVUS guided- and non-guided EIS measurements, the mean values of the impedance magnitude (kΩ) in oxLDL-laden plaque were elevated as compared to the control (Figure 4A & B). The non-IVUS-guided EIS harbored a wide range of magnitude values, with the lower limits overlapping with those of control (Figure 4A), likely from misalignment with the plaque. As a random measurement, EIS at Sites 2 and 3 aligned with the lesion, resulting distinct impedance magnitude, whereas EIS measurement at Site 1 (lesion free) was indistinct from the control. In the case of IVUS-guided measurement, the EIS measurements were aligned with the lesions, resulting in increased frequency-dependent separation from those of control across the entire frequency range (100 Hz – 300 kHz) (Figure 4B).

In addition to the impedance magnitude, the phase (ϕ) spectra provided an alternative detection for the oxLDL-laden lesions (Figure 4C & D). As supported by Eq. (5), the phase of all the measurements overlapped at high frequencies (> 20 kHz). In the random

measurements, the phases of lesion sites overlapped with the control (Figure 4C), while in the guided measurement the lesion sites were distinct at < 15 kHz (Figure 4D).

Statistical analysis demonstrated the EIS measurements with and without IVUS guidance (Figure 5). In the case without IVUS guidance, impedance magnitude (kΩ) at Sites 2 & 3 was distinct from control ($p < 0.0001$ for either A or B), whereas measurement at Site 1 was insignificant ($p < 0.2$). EIS measurements were statistically insignificant considering all results (Figure 5A). IVUS-guided EIS measurements demonstrated statistically significant differences with the added advantage of smaller data spread in a given condition leading to smaller standard deviations (average of 0.54 kΩ for guided and 1.04 kΩ for non-guided measurements) (Figure 5A). Phase delay, an alternative measure derived from EIS, demonstrated similar trends (Figure 5B). Significant statistics were observed at < 20 kHz with IVUS-guidance, whereas insignificance exhibited throughout the frequency range without IVUS-guidance except 2 – 15 kHz range.

4 Discussion

The novelty of the current work resides in the integrated sensor design to enable IVUS-guided EIS assessment of metabolically unstable plaque. The double-layer catheter allowed for the flexible 2-point electrode to affix to the balloon anchored to the outer catheter while the rotating ultrasonic transducer was deployed to the inner catheter. The imaging window distal to the balloon provided matched acoustic impedance, enabling the high-frequency transducer (45 MHz) to visualize the vessel lumen and 2-point electrode to align with the plaques. Thus, we introduced the first IVUS-guided EIS sensor to detect intraplaque oxLDL with reduced standard deviation (from 1.04 to 0.54 kΩ on average for magnitude) and increased statistical significance (from $p < 0.07$ to $p < 0.0001$ for magnitude) compared to non-guided results [15, 41, 53]. Prior to deployment *in vivo*, the sensors were heparinized in 1000 U/ml heparin to minimize adverse interactions between the sensor and blood. Our prior *in vivo* EIS measurements have demonstrated signal stability in the presence of blood (Supplementary file).

The integrated sensor strategy paved the way to diagnose vulnerable plaques to predict acute coronary events or stroke [17, 54]. The non-guided EIS measurements require repeated trials at multiple sites in need of deflating and re-inflating of the balloon, prolonging procedure time with possible fluoroscopy X-rays exposure [55], whereas the IVUS imaging prior to EIS measurement visualizes the anatomy to enable precise alignment with lesions for EIS measurement by single inflation. Statistically significant results were obtained by the IVUS-guided EIS measurement ($p < 0.0001$ for magnitude and $p < 0.005$ for phase within 15 kHz), whereas measurements without the guidance reduced the significance ($p < 0.07$ for magnitude and $p < 0.4$ within 15 kHz) (Figure 5). Without guidance, measurement at random sites caused large variation and low significance in existing publications as well, where lower boundary of lesion sites overlapped the upper boundary of control [15, 41].

Despite significant consistency and reliability, the current design is subjected to improvement. To establish a simultaneous IVUS guided EIS measurement, the inner, outer catheters, as well as the gap between them have to be acoustically transparent. Water instead

of air would be used to inflate the balloon. Currently, the outer catheter is not transparent enough for an acoustic window of the ultrasonic transducer. In addition, fractional flow reserve (FFR) [56, 57] can be incorporated for the future design. A triad of intravascular shear stress (ISS) and electrochemical impedance spectroscopy (EIS) would allow initial identification by disturbed shear, followed by visualization by IVUS, and then electrochemical characterization by EIS, providing patient-specific intervention. Additionally, the current 2-electrode EIS provide certain quantitative evaluation of the plaque severity [41]. Nevertheless, this sensor does not generate detailed quantitative information, such as plaque morphology and 3-dimensional oxLDL concentration. Electrochemical impedance tomography using 32 electrodes are being developed in our group for detailed quantitation.

Percutaneous coronary intervention (PCI) serves as standard of care clinically. Using the minimally invasive technique, the integrated sensor evaluates plaque vulnerability when plaques are detected by non-invasive techniques. This integrated sensor provides a reliable and consistent assessment of oxLDL laden plaques, and estimate of potential clinical events such as coronary syndromes or stroke [17, 54]. Compared to standard PCI which blocks the blood flow for about 10 – 400 seconds (usually within 90 seconds) [58–60], this integrated sensor scans the spectrum at 40 frequencies within 60 seconds. In actual measurement, impedance measurement at one or two frequencies (for example, 100 kHz) is sufficient to distinguish vulnerable plaques from healthy endothelium, which can be accomplished with a few seconds. Compared with non-guided EIS measurements that have to repeat measurements at various sites (about 5 minutes).

5 Conclusion

We introduced integrated IVUS and EIS sensors for an accurate and reliable strategy to characterize intraplaque oxLDL. The IVUS imaging window and the EIS sensor are spatially separated in the double layer catheter design for an effective acoustic window and elimination of interference between the two sensors. The IVUS-guided EIS ensured specifically targeted measurements at the lesion sites, and consequently resulted in high consistency and significance of the electrical impedance. Thus, the dual sensor strategy holds the potential for precision medicine.

Supplementary Material

Refer to Web version on PubMed Central for supplementary material.

Acknowledgments

The Authors acknowledge the support by the National Institute of Heath grants R01HL083015 (TKH), R01HL118650 (TKH), R01HL129727 (TKH), R01HL111437 (TKH), U54 EB022002 (QZ, KKS), P41-EB02182 (QZ, KKS), U54 EB022002 (AB).

Biographies

Jianguo Ma received his Ph.D. in Mechanical Engineering (major) and Electrical Engineering (minor) from North Carolina State University under Dr. Xiaoning Jiang’s

supervision in 2014. He is currently a research scientist in Dr. Tzung K. Hsiai's lab in Department of Bioengineering and Department of Medicine in University of California, Los Angeles. His research interests are instrument technologies on ultrasonic transducers, high resolution light sheet fluorescence microscopy, microwave devices, and their applications on medical diagnosis/therapy and non-destructive evaluations.

Yuan Luo receives his Ph. D in Electronic and Computer Engineering from the Hong Kong University of Science and Technology. He is currently a postdoctoral researcher in Caltech MEMS Lab. at California Institute of Technology. His research interests include micro-engineering, biomedical microdevices, and electrical impedance tomography for clinical applications.

René R. Sevag Packard received his M.D. from the University of Geneva, Switzerland. Following a vascular biology research fellowship at the Brigham and Women's Hospital of Harvard Medical School in Boston, Massachusetts, he completed internal medicine residency training at the University Hospitals of Cleveland of Case Western Reserve University and cardiology fellowship and advanced cardiac imaging training at the Ronald Reagan UCLA Medical Center of the University of California, Los Angeles. He is currently a Ph.D. candidate in the Department of Molecular, Cellular and Integrative Physiology at UCLA in the laboratory of Professor Tzung K. Hsiai. His research interest lies in the application of imaging and bioengineering approaches to help elucidate biological processes at play in cardiovascular diseases such as atherosclerosis and cardiomyopathies.

Teng Ma received his B.S.E degree from University of Michigan, Ann Arbor, USA majoring in Biomedical Engineering in 2011. He received his M.S. degree and Ph.D degree in Biomedical Engineering from University of Southern California, Los Angeles, USA in 2013 and 2015. He joined NIH Resource Center for Medical Ultrasonic Transducer Technology as a Research Assistant and Ph.D. candidate under supervision of Dr. K. Kirk Shung and Dr. Qifa Zhou. In 2013, two of his papers were selected as "Best Student Paper Finalist" and featured in the 2013 Joint UFFC, EFTF and PFM Symposium. His research interests include medical ultrasound technology and multi-modality intravascular imaging by combining ultrasonic and optical techniques, such as intravascular ultrasound (IVUS), intravascular optical coherence tomography (IV-OCT), intravascular photoacoustic imaging (IVPA), and acoustic radiation force optical coherence elastography (ARF-OCE). He is also actively working in translational research and medical device commercialization with entrepreneurial spirit to translate innovative technology from research to clinical benefits.

Yichen Ding is currently a project scientist at the David Geffen School of Medicine, UCLA. Dr. Ding received his Ph.D. in Department of Biomedical Engineering, Peking University in 2015, and B.S. Degree in Department of Precision Instrument, Tsinghua University in 2010, respectively. His research interest is biomedical imaging, especially optical imaging, including optical microscopy (light-sheet, confocal and phase contrast), super-resolution nanoscopy, fluorescent molecular tomography and photoacoustic tomography.

Parinaz Abiri is an MSTP student at the University of California, Los Angeles. She is pursuing her MD at the David Geffen School of Medicine and her PhD in the department of

Bioengineering under the supervision of Dr. Tzung Hsiai. Her research interests currently include the development of medical devices, including diagnostic, surgical, and implantable therapeutic devices.

Yu-Chong Tai is the Anna L. Rosen Professor of Electrical Engineering and Mechanical Engineering and the Executive Officer of the newly founded Medical Engineering at Caltech. He received his B.S. degree in Electrical Engineering from the National Taiwan University, and M.S. and Ph.D. degrees in Electrical Engineering from University of California at Berkeley. After PhD, he joined California Institute of Technology and his research has mainly focused on Micro-Electro-Mechanical Systems (MEMS), microfluidics, lab-on-a-chips, and micro implantable biomedical devices. He was the co-chairman of the 2002 IEEE MEMS Conference. He was elected an IEEE Fellow in 2006. He is also a senior member of the American Society of Mechanical Engineers (ASME).

Qifa Zhou received his Ph. D. degree from the Department of Electronic Materials and Engineering of Xi'an Jiaotong University, China in 1993. He is currently a Research Professor at the NIH Resource on Medical Ultrasonic Transducer Technology and the Department of Biomedical Engineering and Industry & System Engineering at the University of Southern California (USC), Los Angeles, *CA*. Before joining USC in 2002, he worked in the Department of Physics at Zhongshan University in China, the Department of Applied Physics, Hong Kong Polytechnic University, and the Materials Research Laboratory, Pennsylvania State University. Dr. Zhou is a fellow of International Society for Optics and Photonics (SPIE) and American Institute for Medical and Biological Engineering (AIMBE). He is also a senior member of the IEEE Ultrasonics, Ferroelectrics, and Frequency Control (UFFC) Society and a member of the UFFC Society's Ferroelectric Committee. He is a member of the Technical Program Committee of the IEEE International Ultrasonics Symposium. He is an Associate Editor of the *IEEE Transactions on Ultrasonics, Ferroelectrics, and Frequency Control.* His current research interests include the development of ferroelectric thin films, MEMS technology, nano-composites, and modeling and fabrication of high-frequency ultrasound transducers and arrays for medical imaging applications, such as photoacoustic imaging and intravascular imaging. He has published more than 130 journal papers in this area.

K. Kirk Shung is a dean's professor in biomedical engineering at University of Southern California. He is a life fellow of IEEE and has received many awards including the Holmes Pioneer Award in Basic Science from American Institute of Ultrasound in Medicine in 2010 and the academic career achievement award from the IEEE Engineering in Medicine and Biology Society in 2011. He is the recipient of 2016 IEEE Biomedical Engineering Award. Dr. Shung has published more than 500 papers and book chapters. He is the author of a textbook "Principles of Medical Imaging" published by Academic Press in 1992 and two editions of a textbook "Diagnostic Ultrasound: Imaging and Blood Flow Measurements" published by CRC press in 2005 and 2015. Dr. Shung is currently serving as an associate editor of IEEE Transactions on Biomedical and Engineering, IEEE Transactions on Ultrasonics, Ferroelectrics and Frequency Control, and Medical Physics.

Rongsong Li is an associate adjunct professor at University of California Los Angeles. He received his Ph.D. degree from Tufts University. Dr. Li's research interests focus on the effects and mechanisms of risk factors such as particulate matter in air pollutant, shear stress and oxidized lipids on vascular diseases.

Tzung K. Hsiai is the Professor of Medicine (Cardiology) and Bioengineering. He received his undergraduate education from Columbia University and his MD from the University of Chicago. He completed his internship, residency and NIH-funded cardiovascular fellowship at UCLA School of Medicine, where he pursued interdisciplinary research in BioMEMS and vascular biology. His group's research focuses on flexible sensors to study mechano-signal transduction of cardiovascular diseases. His group has developed the quantitative approach to monitor intravascular shear stress and vascular oxidative stress to assess unstable plaque. His transdisciplinary research program has been enriched by collaboration with UCLA Wireless Health Institute, Medical Imaging Informatics, Atherosclerosis Research Unit, Cardiovascular Research Lab, Cellular, Molecular and Developmental Biology, and UCLA Center for Human Nutrition. He is the Chair of the American Physiological Society Joint Meeting with Biomedical Engineering Society, Member of the American Society for Clinical Investigation, Member of National Institutes of Health Bioengineering, Biotechnology, and Surgical Science Study Section, Fellow of American College of Cardiology, American Heart Association, and the recipient of an American Heart Association John J. Simpson Outstanding Research Achievement Award and UCLA SEAS Distinguished Young Alumnus Award.

References

1. Madamanchi NR, Vendrov A, Runge MS. Oxidative stress and vascular disease. Arterioscl Throm Vas. 2005; 25:29–38.
2. Davies PF, Remuzzi A, Gordon EJ, Dewey CF, Gimbrone MA. Turbulent fluid shear stress induces vascular endothelial cell turnover in vitro. P Natl Acad Sci. 1986; 83:2114–2117.
3. Bamford J, Sandercock P, Dennis M, Warlow C, Burn J. Classification and natural history of clinically identifiable subtypes of cerebral infarction. The Lancet. 1991; 337:1521–1526.
4. Virmani R, BURKE AP, KOLODGIE FD, Farb A. Vulnerable plaque: the pathology of unstable coronary lesions. J Interv Cardiol. 2002; 15:439–446. [PubMed: 12476646]
5. Virmani R, Burke AP, Farb A, Kolodgie FD. Pathology of the unstable plaque. Prog Cardiovasc Dis. 2002; 44:349–356. [PubMed: 12024333]
6. Worthley SG, Helft G, Fuster V, Fayad ZA, Shinnar M, Minkoff LA, et al. A novel nonobstructive intravascular MRI coil in vivo imaging of experimental atherosclerosis. Arterioscl Throm Vas. 2003; 23:346–350.
7. Vallabhajosula S, Fuster V. Atherosclerosis: imaging techniques and the evolving role of nuclear medicine. J Nucl Med. 1997; 38:1788. [PubMed: 9374357]
8. Fayad Z, Fuster V. Clinical imaging of the high-risk or vulnerable atherosclerotic plaque. Circ Res. 2001; 89:305–316. [PubMed: 11509446]
9. Jaffer FA, Vinegoni C, John MC, Aikawa E, Gold HK, Finn AV, et al. Real-time catheter molecular sensing of inflammation in proteolytically active atherosclerosis. Circulation. 2008; 118:1802–1809. [PubMed: 18852366]
10. Marcu L, Fishbein MC, Maarek J-MI, Grundfest WS. Discrimination of human coronary artery atherosclerotic lipid-rich lesions by time-resolved laser-induced fluorescence spectroscopy. Arterioscl Throm Vas. 2001; 21:1244–1250.

11. Finn AV, Nakano M, Narula J, Kolodgie FD, Virmani R. Concept of vulnerable/unstable plaque. Arterioscl Throm Vas. 2010; 30:1282–1292.
12. Kim D-H, Lu N, Ma R, Kim Y-S, Kim R-H, Wang S, et al. Epidermal electronics. Science. 2011; 333:838–843. [PubMed: 21836009]
13. Rouhanizadeh, M.; Tang, T.; Li, C.; Soundararajan, G.; Zhou, C.; Hsiai, T. Applying indium oxide nanowires as sensitive and selective redox protein sensors. 2004 17th IEEE Intl Conf MEMS, IEEE2004; p. 434-437.
14. Hwang J, Rouhanizadeh M, Hamilton RT, Lin TC, Eiserich JP, Hodis HN, et al. 17β-Estradiol reverses shear-stress-mediated low density lipoprotein modifications. Free Radical Bio Med. 2006; 41:568–578. [PubMed: 16863990]
15. Yu F, Dai X, Beebe T, Hsiai TK. Electrochemical impedance spectroscopy to characterize inflammatory atherosclerotic plaques. Biosens Bioelectron. 2011; 30:165–173. [PubMed: 21959227]
16. Ai L, Rouhanizadeh M, Wu JC, Takabe W, Yu H, Alavi M, et al. Shear stress influences spatial variations in vascular Mn-SOD expression: implication for LDL nitration. Am J Physiol-Cell Ph. 2008; 294:C1576–C1585.
17. Yu F, Li R, Ai L, Edington C, Yu H, Barr M, et al. Electrochemical Impedance Spectroscopy to Assess Vascular Oxidative Stress. Ann Biomed Eng. 2011; 39:287–296. [PubMed: 20652746]
18. Cao H, Yu F, Zhao Y, Scianmarello N, Lee J, Dai W, et al. Stretchable electrochemical impedance sensors for intravascular detection of lipid-rich lesions in New Zealand White rabbits. Biosens Bioelectron. 2014; 54:610–616. [PubMed: 24333932]
19. Kolodgie FD, Burke AP, Farb A, Gold HK, Yuan J, Narula J, et al. The thin-cap fibroatheroma: a type of vulnerable plaque: the major precursor lesion to acute coronary syndromes. Curr Opin Cardiol. 2001; 16:285–292. [PubMed: 11584167]
20. Virmani R, Burke AP, Farb A, Kolodgie FD. Pathology of the vulnerable plaque. J Am Coll Cardiol. 2006; 47:C13–C18. [PubMed: 16631505]
21. Puri R, Worthley MI, Nicholls SJ. Intravascular imaging of vulnerable coronary plaque: current and future concepts. Nat Rev Cardiol. 2011; 8:131–139. [PubMed: 21263456]
22. Doyle B, Caplice N. Plaque neovascularization and antiangiogenic therapy for atherosclerosis. J Am Coll Cardiol. 2007; 49:2073–2080. [PubMed: 17531655]
23. Khurana R, Simons M, Martin JF, Zachary IC. Role of angiogenesis in cardiovascular disease a critical appraisal. Circulation. 2005; 112:1813–1824. [PubMed: 16172288]
24. Li X, Li J, Jing J, Ma T, Liang S, Zhang J, et al. Integrated IVUS-OCT imaging for atherosclerotic plaque characterization. IEEE J Sel Top Quant. 2014; 20:196–203.
25. Wang LV. Multiscale photoacoustic microscopy and computed tomography. Nat photonics. 2009; 3:503–509. [PubMed: 20161535]
26. Wang LV, Hu S. Photoacoustic tomography: in vivo imaging from organelles to organs. Science. 2012; 335:1458–1462. [PubMed: 22442475]
27. Xu M, Wang LV. Photoacoustic imaging in biomedicine. Rev Sci Instrum. 2006; 77:041101.
28. Wang B, Su JL, Karpiouk AB, Sokolov KV, Smalling RW, Emelianov SY. Intravascular photoacoustic imaging. IEEE J Sel Top Quant. 2010; 16:588–599.
29. Jansen K, Van Der Steen AF, van Beusekom HM, Oosterhuis JW, van Soest G. Intravascular photoacoustic imaging of human coronary atherosclerosis. Opt Lett. 2011; 36:597–599. [PubMed: 21368919]
30. Wang B, Su JL, Amirian J, Litovsky SH, Smalling R, Emelianov S. Detection of lipid in atherosclerotic vessels using ultrasound-guided spectroscopic intravascular photoacoustic imaging. Opt Express. 2010; 18:4889–4897. [PubMed: 20389501]
31. Stefanadis C, Diamantopoulos L, Vlachopoulos C, Tsiamis E, Dernellis J, Toutouzas K, et al. Thermal Heterogeneity Within Human Atherosclerotic Coronary Arteries Detected In Vivo A New Method of Detection by Application of a Special Thermography Catheter. Circulation. 1999; 99:1965–1971. [PubMed: 10208999]
32. Weissleder R, Tung C-H, Mahmood U, Bogdanov A. In vivo imaging of tumors with protease-activated near-infrared fluorescent probes. Nat Biotechnol. 1999; 17:375–378. [PubMed: 10207887]

33. Rudd JH, Warburton E, Fryer T, Jones H, Clark J, Antoun N, et al. Imaging atherosclerotic plaque inflammation with [18F]-fluorodeoxyglucose positron emission tomography. Circulation. 2002; 105:2708–2711. [PubMed: 12057982]
34. Gessner R, Lukacs M, Lee M, Cherin E, Foster FS, Dayton P. High-resolution, high-contrast ultrasound imaging using a prototype dual-frequency transducer: in vitro and in vivo studies. IEEE T Ultrason Ferr. 2010; 57:1772–1781.
35. Gessner RC, Frederick CB, Foster FS, Dayton PA. Acoustic angiography: a new imaging modality for assessing microvasculature architecture. J Biomed Imaging. 2013; 2013:14.
36. Lindner JR, Song J, Jayaweera AR, Sklenar J, Kaul S. Microvascular rheology of Definity microbubbles after intra-arterial and intravenous administration. J Am Soc Echocardiog. 2002; 15:396–403.
37. Lindner JR. Microbubbles in medical imaging: current applications and future directions. Nat Rev Drug Discov. 2004; 3:527–533. [PubMed: 15173842]
38. Ma J, Martin KH, Dayton P, Jiang X. A preliminary engineering design of intravascular dual-frequency transducers for contrast-enhanced acoustic angiography and molecular imaging. IEEE T Ultrason Ferr. 2014; 61:870–880.
39. Ma J, Martin KH, Li Y, Dayton PA, Shung KK, Zhou Q, et al. Design factors of intravascular dual frequency transducers for super-harmonic contrast imaging and acoustic angiography. Phys Med Biol. 2015; 60:3441. [PubMed: 25856384]
40. Ma J, Steer MB, Jiang X. An acoustic filter based on layered structure. Appl Phys Lett. 2015; 106:111903. [PubMed: 25829548]
41. Packard R, Zhang X, Luo Y, Ma T, Jen N, Ma J, et al. Two-point stretchable electrode array for endoluminal electrochemical impedance spectroscopy measurements of lipid-laden atherosclerotic plaques. Ann Biomed Eng. 2016
42. Ma T, Zhou B, Hsiai TK, Shung KK. A Review of Intravascular Ultrasound–Based Multimodal Intravascular Imaging The Synergistic Approach to Characterizing Vulnerable Plaques. Ultrasonic Imaging. 2015 0161734615604829.
43. Elliott M, Thrush A. Measurement of resolution in intravascular ultrasound images. Physiol Meas. 1996; 17:259. [PubMed: 8953624]
44. Brezinski ME, Tearney GJ, Weissman N, Boppart S, Bouma B, Hee M, et al. Assessing atherosclerotic plaque morphology: comparison of optical coherence tomography and high frequency intravascular ultrasound. Heart. 1997; 77:397–403. [PubMed: 9196405]
45. Yu F, Lee J, Jen N, Li X, Zhang Q, Tang R, et al. Elevated electrochemical impedance in the endoluminal regions with high shear stress: Implication for assessing lipid-rich atherosclerotic lesions. Biosens Bioelectron. 2013; 43:237–244. [PubMed: 23318546]
46. Li X, Ma T, Tian J, Han P, Zhou Q, Shung KK. Micromachined PIN-PMN-PT crystal composite transducer for high-frequency intravascular ultrasound (IVUS) imaging. IEEE T Ultrason Ferr. 2014; 61:1171–1178.
47. Larsson J. Electromagnetics from a quasistatic perspective. Am J Phys. 2007; 75:230–239.
48. Anichkov N, Volkova K. Reactive modifications of structural elements of the aortic wall in rabbit in experimental lipoidosis. Arkhiv anatomii, gistologii i embriologii. 1954; 32:41–47.
49. Anichkov N. Present state of experimental atherosclerosis. Vestnik Akademii meditsinskikh nauk SSSR. 1955; 11:13–24.
50. Anitschkow N, Chalatow S, PELIAS M. On experimental cholesterin steatosis and its significance in the origin of some pathological processes. Arteriosclerosis. 1983; 3:178–182. [PubMed: 6340651]
51. Srivastava SK, Artemiou A, Minerick AR. Direct current insulator-based dielectrophoretic characterization of erythrocytes: ABO-Rh human blood typing. Electrophoresis. 2011; 32:2530–2540. [PubMed: 21922495]
52. Sokal, RR.; Rohlf, FJ. Introduction to Biostatistics. 2. New York: Dover Publications; 1987.
53. Cho, S. Proc EU-Korea Conf Sci Tech. Springer; 2008. Electrical Impedance Spectroscopy for Intravascular Diagnosis of Atherosclerosis; p. 395-403.

54. Ehara S, Ueda M, Naruko T, Haze K, Itoh A, Otsuka M, et al. Elevated levels of oxidized low density lipoprotein show a positive relationship with the severity of acute coronary syndromes. Circulation. 2001; 103:1955–1960. [PubMed: 11306523]

55. Geijer H, Persliden J. Radiation exposure and patient experience during percutaneous coronary intervention using radial and femoral artery access. Eur Radiol. 2004; 14:1674–1680. [PubMed: 15103500]

56. Pijls NH, de Bruyne B, Peels K, van der Voort PH, Bonnier HJ, Bartunek J, et al. Measurement of fractional flow reserve to assess the functional severity of coronary-artery stenoses. New Eng J Med. 1996; 334:1703–1708. [PubMed: 8637515]

57. Watkins S, McGeoch R, Lyne J, Steedman T, Good R, McLaughlin M-J, et al. Validation of magnetic resonance myocardial perfusion imaging with fractional flow reserve for the detection of significant coronary heart disease. Circulation. 2009; 120:2207–2213. [PubMed: 19917885]

58. Garrido IP, Roy D, Calviño R, Vazquez-Rodriguez JM, Aldama G, Cosin-Sales J, et al. Comparison of ischemia-modified albumin levels in patients undergoing percutaneous coronary intervention for unstable angina pectoris with versus without coronary collaterals. Am J Cardiol. 2004; 93:88–90. [PubMed: 14697474]

59. Laskey WK. Brief repetitive balloon occlusions enhance reperfusion during percutaneous coronary intervention for acute myocardial infarction: a pilot study. Catheter Cardio Inte. 2005; 65:361–367.

60. Laskey WK, Yoon S, Calzada N, Ricciardi MJ. Concordant improvements in coronary flow reserve and ST-segment resolution during percutaneous coronary intervention for acute myocardial infarction: A benefit of postconditioning. Catheter Cardio Inte. 2008; 72:212–220.

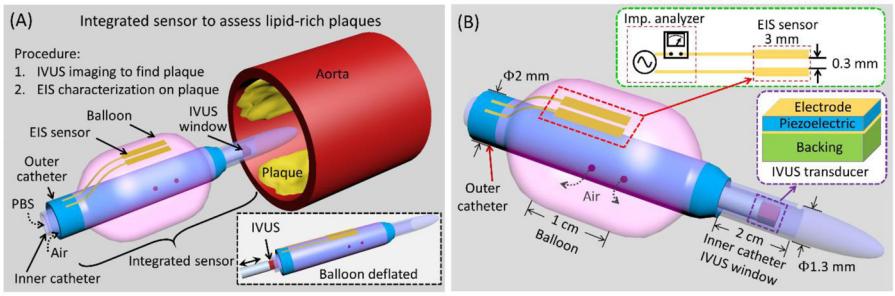

Figure 1.

(**A**) Conceptual scheme depicts the deployment of the integrated sensor consisting of an EIS sensor and an IVUS transducer to assess lipid-rich plaques. The IVUS sensor visualizes the aorta lumen, and the imaging information provides guidance for EIS characterization of the plaques by aligning the EIS sensor (2-point electrode) at the plaque. PBS: Phosphate-buffered saline solution. (**B**) The design of the integrated sensor highlights the mechanism for IVUS-guided EIS measurement. The IVUS transducer is positioned inside the inner catheter (ID: 1 mm, OD: 1.3 mm) with an imaging window of 2 cm to 10 cm. The EIS sensor is affixed to the balloon, which is anchored to the outer catheter (ID: 1.7 mm, OD: 2 mm). External pump generates air pressure to inflate or deflate the balloon, ranging from 2.3 mm to 6 mm in diameter.

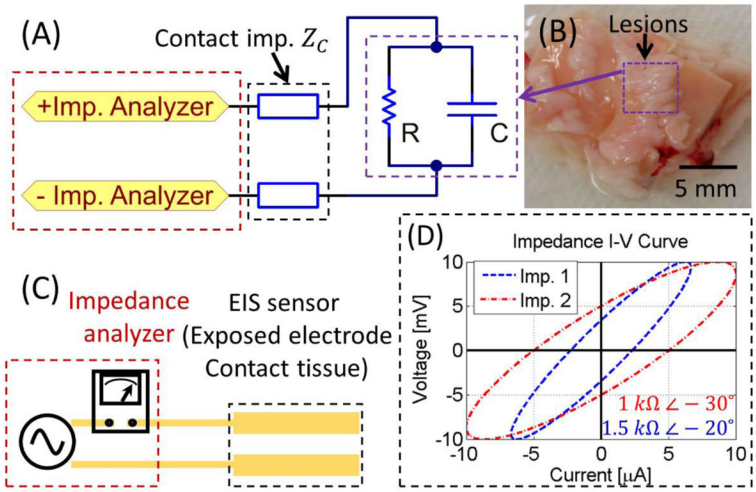

Figure 2.

(**A**) Schematic representation of the equivalent circuit for EIS measurement. (**B**) In an EIS system, the EIS sensor (exposed electrode) is attached to the specimen (e.g. aorta covered by plaques). (**C**) The impedance is recorded by an impedance analyzer, as illustrated by **(D)** the current-voltage (I–V) curve to provide both magnitude and phase delay.

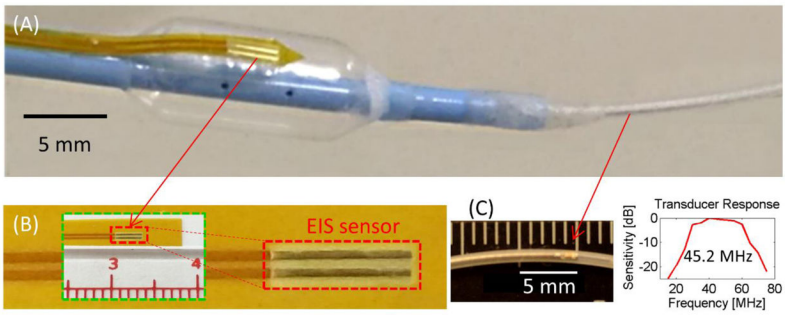

Figure 3.

A prototype of the integrated sensor. (**A**) The photograph of the integrated sensor highlighted the relative position of the EIS sensor and the ultrasonic transducer. (**B**) Zoom-in of the EIS sensor illustrated the polyimide substrate for flexibility. (**C**) Zoom-in of the IVUS transducer inside the inner catheter and its frequency responses.

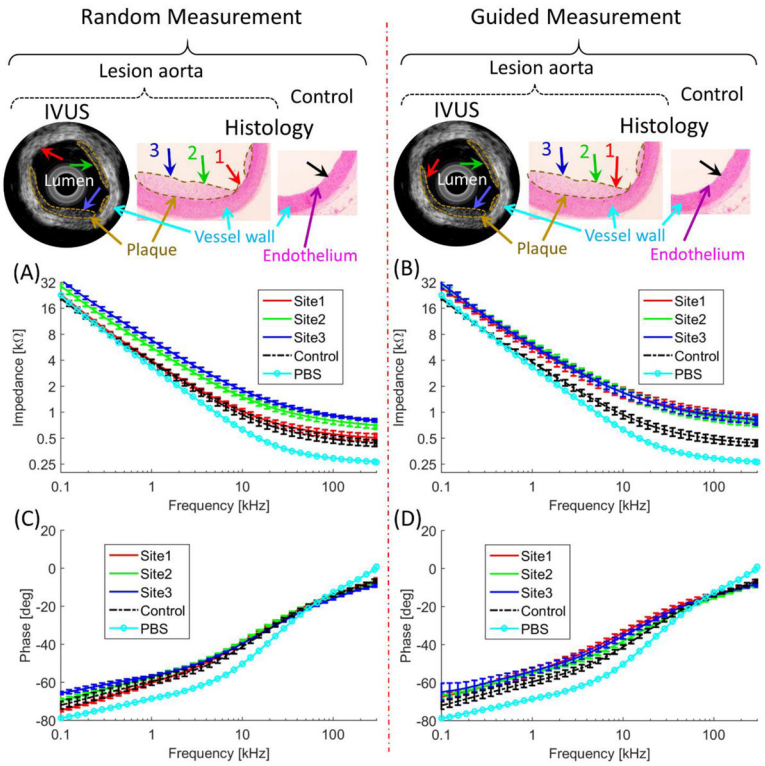

Figure 4.

Performances of the integrated transducer were demonstrated by comparing random (non-guided) and guided-measurements. Without the guidance, the EIS measurements at Site 1 missed the lesions (red arrow). With the IVUS guidance, EIS measurement sites were aligned with Sites 1, 2, and 3 (red, green, and blue arrow). (A) and (B) illustrated EIS measurement in terms of impedance magnitude, (C) and (D) the phase spectra. **(A)** Frequency-dependent impedance (kΩ) increased between 100 Hz to 300 kHz in the oxLDL-laden aorta (red, green, and blue) versus the lesion-free aorta (control, black). (**B**) With the IVUS guidance, the frequency-dependent impedance (red, green, and blue arrows) significantly increased between 100 Hz to 300 kHz as compared to the control (black). (**C**) The phase spectrum was indistinct in the random measurements from 100 Hz to 300 kHz. (**D**) With the guidance, the phase was distinct from the control at < 15 kHz.

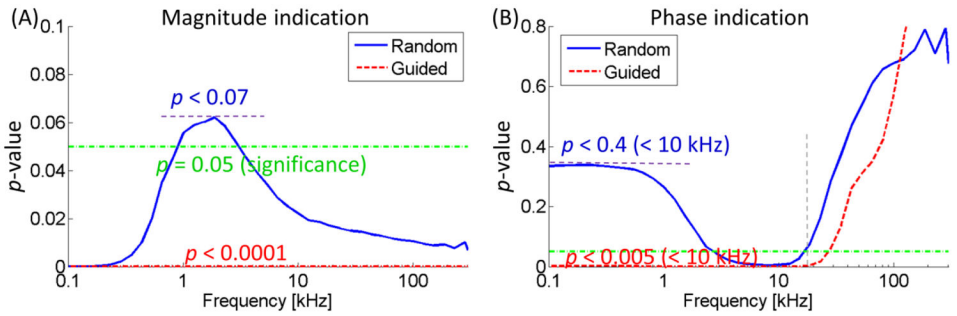

Figure 5.

(**A**) Statistical analysis of the magnitude measurements. (**B**) The random measurements resulted in insignificant result ($p < 0.4$) while the guided measurement resulted in significant result ($p < 0.005$) at < 15 kHz). At high frequencies (> 20 kHz), even guided measurements were statistically insignificant.

Table 1

Comparison of individual versus integrated intravascular modalities.

Histopathology\Modalities	OCT	IVUS	NIRF	^{18}FGD-PET	EIS	IVUS-EIS
Thin-cap fibroatheroma	X	X				**X**
Fibrous structure		X				**X**
Calcification		X			X	**X**
Oxidize LDL/foam cells					X	**X**
Protease activity			X			
Glucose analogue				X		

OCT: optical coherence tomography; IVUS: intravascular ultrasound; NIRF: near inferred fluorescence; ^{18}FGD-PET: ^{18}F-fluorodexygluecose positron emission tomography; IVUS-EIS: an integrated EIS probe guided by high frequency intravascular ultrasound.

Sens Actuators B Chem. Author manuscript; available in PMC 2017 November 01.